Editors' Suggestion

Volatile two-dimensional electron gas in ultrathin $BaTiO_3$ films

Peter Lutz,[1] Simon Moser,[2,*] Vedran Jovic,[2] Young Jun Chang,[2,3] Roland J. Koch,[2] Søren Ulstrup,[2] Ji Seop Oh,[2,4,5] Luca Moreschini,[2] Sara Fatale,[6] Marco Grioni,[6] Chris Jozwiak,[2] Aaron Bostwick,[2] Eli Rotenberg,[2] Hendrik Bentmann,[1] and Friedrich Reinert[1]

[1]*Experimentelle Physik VII, Röntgen Research Center for Complex Materials (RCCM), Universität Würzburg, Am Hubland, D-97074 Würzburg, Germany*

[2]*Advanced Light Source (ALS), Berkeley, California 94720, USA*

[3]*Department of Physics, University of Seoul, Seoul 02504, Republic of Korea*

[4]*Center for Correlated Electron Systems, Institute for Basic Science, Seoul 08826, Korea*

[5]*Department of Physics and Astronomy, Seoul National University, Seoul 08826, Korea*

[6]*Institute of Physics (IPHYS), Ecole Polytechnique Federale de Lausanne (EPFL), CH-1015 Lausanne, Switzerland*

(Received 10 May 2017; revised manuscript received 9 July 2017; published 28 September 2018)

We investigate the metallic surface state in ultrathin films of $BaTiO_3$ by angle-resolved photoemission spectroscopy. We find Fermi-surface contours derived from the Ti $3d$ t_{2g} conduction band, similar as in $SrTiO_3$ but with broader spectral features due to enhanced quasiparticle scattering. Oxygen vacancies created in the x-ray beam spot allow for reversible *in situ* doping control up to surface carrier densities as high as 10^{14} cm^{-2}, but vacancy migration into the subsurface at $T \geqslant 285$ K quenches the surface state. Our analysis suggests that the charge state of oxygen vacancies in ultrathin films is predominantly 2+, which limits charge-carrier trapping and the formation of localized defect states.

DOI: 10.1103/PhysRevMaterials.2.094411

Introduction.—Barium titanate ($BaTiO_3$, BTO) is an important ferroelectric material with a high transition temperature ($T_c = 390$ K) and excellent dielectric and piezoelectric properties [1]. Recently, BTO was hoped to become a nonvolatile and nontoxic (lead-free) alternative to current ferroelectric memories and electro-optic devices. Even though the microscopic origin of ferroelectricity in BTO is still controversial [2], its large ferroelectrically polarized bulk domains at room temperature are useful for a number of innovative microelectronic applications.

In heterostructures, BTO can be combined with other functional oxides [3] to create multifunctional materials with enhanced ferroelectric properties [4], potentially in combination with switchable conductive channels at heterointerfaces [5] and domain walls [6]. By control of the epitaxial strain, the ferroelectric properties can be tuned, and remanent polarization was reportedly enhanced by up to 250%, significantly increasing the transition temperature and allowing for stable room-temperature applications [7]. A ferroelectric field effect in BTO further regulates the charge-carrier density of the underlying substrate [8], whereas an electroresistive effect tunes the tunneling [9,10]—and in combination with ferromagnetic electrodes—even the spin current [11]. With the recent successful integration of BTO epitaxial thin films onto silicon, commercial field-effect transistors, and thin-film capacitors come realistically within reach [12].

Ferroelectricity generally also survives in thin films of BTO [13]. The film thickness, however, affects the transition temperature [14], the orientation, and the switchability of the ferroelectric domains [12]. Electron doping of BTO can lead to similar property changes, but ferroelectricity generally persists up to a critical electron concentration of $\sim 10^{21}$ cm^{-3} [15]. A reliable control of the thickness as well as the doping concentration are thus important prerequisites for the design of robust applications based on BTO.

The most common source of intrinsic—and often times unwanted—doping in BTO is the oxygen defect (V_O) with low formation energies pinning the Fermi level in the bulk close to the conduction band and providing electron doping at room temperature [16]. In thin films, oxygen defects are hardly avoidable and typically introduced during growth under oxygen-poor conditions. The equilibrium of ionized defects and free charge bends the band structure and confines doped-in electrons close to the surface. A two-dimensional electron gas (2DEG) is formed. Recently, such 2DEGs have gained considerable attention and were investigated by angle-resolved photoemission spectroscopy (ARPES) [17–19]. A prominent showcase is $SrTiO_3$ (STO), the paraelectric structural isomorph of BTO. Oxygen vacancies can be created in the focus of an intense x-ray beam [20,21] and populate the Ti $3d$ t_{2g}-derived conduction band up to their charge neutrality level. From this point, the oxygen defects ionize only partially and form localized defect states inside the band gap [22].

Analogous experimental studies in BTO are rare [23–25] and more challenging as large single-oriented crystal domains are typically hard to isolate. Commercial high quality single crystals do not provide sufficient bulk doping, and ordered surfaces are difficult to prepare, hampering reliable ARPES experiments at low defect concentrations. Moreover, the technologically relevant ferroelectric tetragonal phase of BTO stabilizes only above 280 K, and temperature-dependent oxygen

*skmoser@lbl.gov

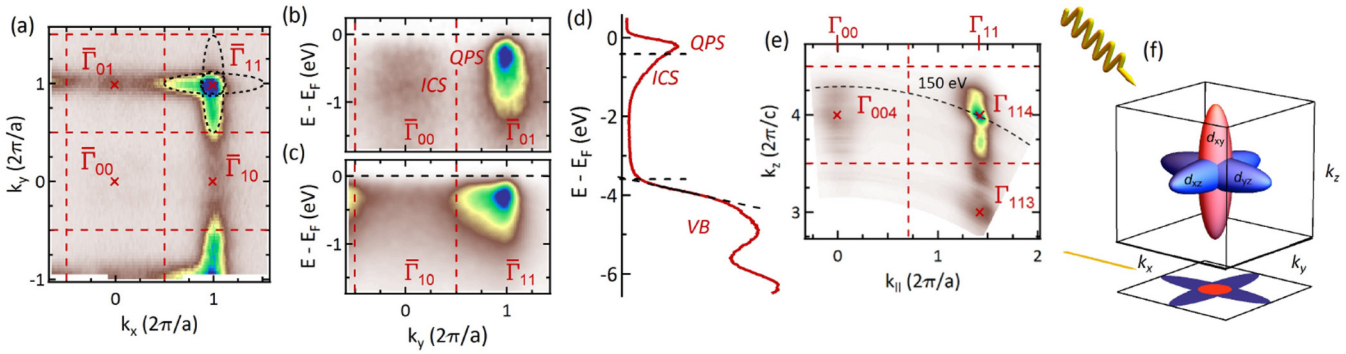

FIG. 1. ARPES overview of an 8-unit-cell BTO thin film. Red dashed lines represent the surface Brillouin zone (BZ) boundaries. (a) Fermi-surface and (b,c) ARPES band-structure maps along representative high-symmetry lines in (a) ($h\nu = 150$ eV, p polarized, $T = 100$ K, and $p = 10^{-11}$ mbar). (d) Energy distribution curve (EDC) of the valence-band (VB) and CB regions. Both VB and CB edges are marked by dashed lines. (e) k_z scan created from ARPES data in the photon energy range of 80 eV $\leqslant h\nu \leqslant$ 180 eV. The black arc indicates the ARPES hemisphere of panel (a). (f) Sketch of the d_{xz}, d_{yz} (blue), and d_{xy} (red) Fermi-surface ellipsoids with respect to the three-dimensional (3D) BZ (black box) and the incoming light. The in-plane projection is shown at the bottom.

defect studies can be obscured by a multitude of structural phase transitions.

Results.—To overcome these obstacles, we choose an alternative experimental approach. Ultrathin (eight unit-cells) epitaxial BTO films are grown on slightly n-doped STO (001) substrates and studied by *in situ* ARPES (see the Supplemental Material [26] for details on sample preparation and characterization). The epitaxial strain at this film thickness pins the crystal structure and exposes large atomically smooth (but not necessarily ferroelectric) domains of unreconstructed tetragonal BTO [12,27]. A dynamic equilibrium in between x-ray beam and oxygen gas exposure during the ARPES experiment stabilizes the V_O concentration at a desired level and allows to continuously and reversibly tune the free surface carrier concentration up to 10^{14} cm^{-2}. A 2DEG with pronounced Fermi-surface contours forms with quasiparticle states (QPSs) revealing the orbital character of the Ti 3d-derived conduction band (CB) with t_{2g} symmetry, similar to what is found in STO. Its incoherent spectral contributions (ICSs) penetrate as far as ∼2 eV into the band gap but retain the delocalized orbital character of the QPS. Pronounced localized in-gap states indicative of partially ionized oxygen vacancies are not observed. We argue this to be the consequence of a peculiarly high charge neutrality level of the twofold ionized oxygen defects in ultrathin BTO films. Our ARPES analysis indeed suggests a prevalent 2+ charge state of oxygen defects, persisting for Fermi levels as high as 0.35 eV above the surface CB edge and thus providing an efficient doping mechanism. However, temperature activates the migration of oxygen defects into the subsurface, which alters the surface potential and quenches the 2DEG around $T \geqslant 285$ K. This needs to be taken into account in the design of nonstoichiometric room-temperature applications based on BTO and other related oxide systems.

2DEG characterization.—Figure 1 gives an ARPES overview of a BTO thin film. Figure 1(a) is a Fermi surface obtained with $h\nu = 150$ eV photons, where the $\overline{\Gamma}_{11}$ point of the surface (BZ, red dashed lines, labeled by Miller indices) coincides with the Γ_{114} point of the bulk BZ. The spectral weight is suppressed at $\overline{\Gamma}_{00}$. At $\overline{\Gamma}_{10}$ we find faint spectral weight elongated along k_y; at $\overline{\Gamma}_{01}$ it is elongated along k_x. At $\overline{\Gamma}_{11}$ we observe distinct intensity contours, indicative of three electron pockets. Ellipsoidal contributions elongated along both k_x and k_y as well as a circular contour are observed. Beyond $k_x \geqslant 2\pi/a$ and $k_y \geqslant 2\pi/a$, the spectral weight fades off.

Panels (b) and (c) show ARPES cuts along prominent high-symmetry directions in (a). Data along $k_x = 0$ in (b) show a broad and ill-defined (FWHM > 0.2 eV) QPS-like feature at $\overline{\Gamma}_{01}$, creating faint contrast in (a). At normal emission $\overline{\Gamma}_{00}$, the QPS is suppressed by matrix elements and exposes ICS, localized in k-space and accumulating at $E - E_F \sim -0.75$ eV. ARPES data cutting along $k_x = 2\pi/a$ in (c) reveals QPS contributions centered at $\overline{\Gamma}_{11}$, forming the ellipsoidal and circular contours in (a). From their areas, we estimate a surface carrier density of $\sim 10^{14}$ cm^{-2}. Panel (d) is an EDC at $\overline{\Gamma}_{11}$ over a wider energy range, exposing the CB, the band gap, and the VB onset at the surface. The CB is composed of QPS and by the ICS tail. Extrapolation of the VB shoulder places the VB edge at $E - E_F \sim -3.55$ eV (black dashed lines). Comparing this value to the band-gap $E_g \sim 3.27$ eV [28] of BTO gives a Fermi level approximately ~ 0.28 eV above the CB edge.

Overall, the distribution of ARPES spectral weight is nonuniform in the individual BZs, reflecting: (i) the symmetry of the initial-state wave function and (ii) the modulation of the photoemission spectral weight in three-dimensional k space. The data are consistent with preliminary results for BTO [23–25] and similar to observations on $SrTiO_3$ [17,18,29] where the Fermi surface is composed of Ti 3d states with t_{2g} symmetry. Due to anisotropic charge-carrier hopping, the d_{xz} (d_{yz}) states form ellipsoidal contours elongated along k_y (k_x) [blue in Fig. 1(f)]. Their orbital nodes suppress spectral weight along the yz (xz) plane [30,31]. The circular contour reflects the d_{xy} states, elongated along k_z [red in Fig. 1(f)] and with orbital nodes (intensity suppression) along both the xz and the yz planes.

The inequivalent intensity distribution of the QPS in adjacent surface BZs is an indicator of the 2DEG wave function to penetrate slightly into the film, causing out-of-plane spectral

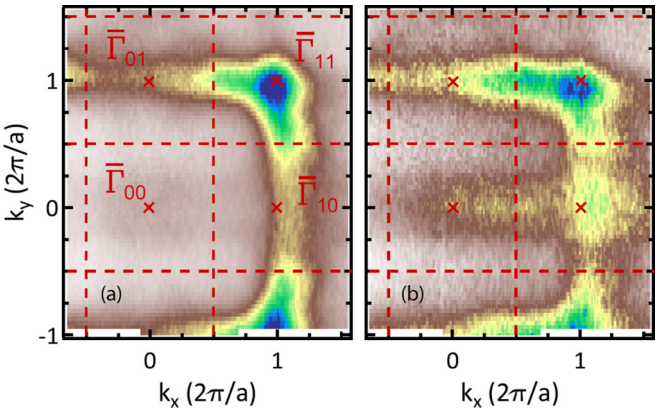

FIG. 2. ARPES constant energy maps at (a) $E - E_F = -1$ eV and (b) $E - E_F = -1.75$ eV ($h\nu = 150$ eV, p polarized, $T = 100$ K, $p = 10^{-11}$ mbar). The spectral weight distribution of the ICS is similar to the distribution of the QPS in Fig. 1(a), indicating their identical orbital characters.

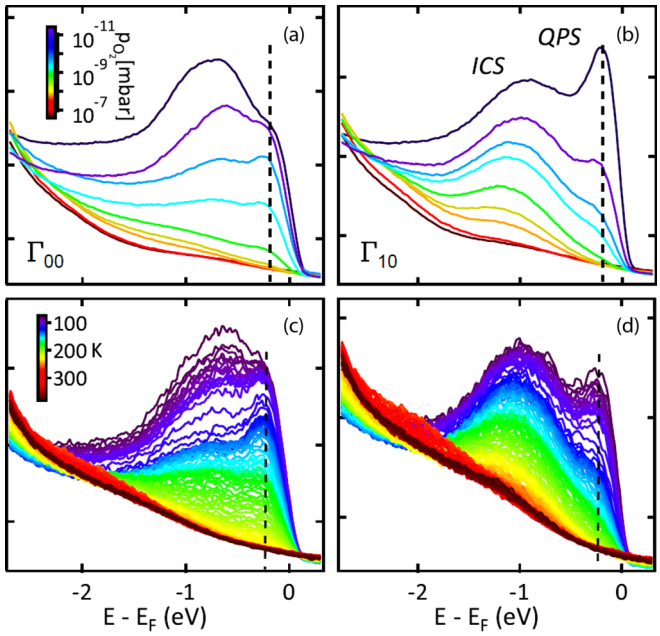

FIG. 3. Normalized EDCs at (a,c) $\overline{\Gamma}_{00}$ and (b,d) $\overline{\Gamma}_{01}$ as a function of oxygen partial pressure at (a,b) $T = 100$ K and as a function of temperature at (c,d) $p = 10^{-11}$ mbar, respectively ($h\nu = 135$ eV).

weight to accumulate throughout the 3D BZ of tetragonal BTO [32]. Figure 1(e) shows a k_z-dependent Fermi surface along the $k_x = k_y$ direction. It is created from ARPES data in the photon energy range of 80 eV $\leqslant h\nu \leqslant$ 180 eV. We observe essentially nondispersive spectral weight at $\overline{\Gamma}_{11}$ with two intensity maxima at the Γ_{113} and the Γ_{114} points of the 3D tetragonal BZ. The latter coincides with $\overline{\Gamma}_{11}$ in panel (a). Despite being much weaker, the spectral weight at normal emission $\overline{\Gamma}_{00}$ forms an elliptical intensity contour close to Γ_{004} and elongated along k_z.

The orbital character of the ICS is explored in Fig. 2. Two constant energy cuts far below the Fermi level at (a) $E - E_F = -1$ eV and (b) $E - E_F = -1.75$ eV are shown. At these energies, the intensity contours represent the ICS part of the spectral function. In both cases, they qualitatively reflect the Fermi-surface contour in Fig. 1(a). This suggests an identical delocalized orbital character of the QPS and the ICS as expected for incoherent spectral contributions.

To summarize, the metallic QPSs in ultrathin films of tetragonal BTO show qualitatively similar signatures as in STO. They are formed from Ti $3d$ t_{2g} orbitals, dispersing strongly along their elongation plane but weakly perpendicular to this plane. Accumulation of spectral weight along k_z indicates multiple BTO layers to contribute to the ARPES signal and the 2DEG wave function to penetrate several unit cells into the film. The broad QPSs are accompanied by a significant amount of ICS contributions, suggesting significant QP scattering, and a QP mass three to five times larger than the band mass of $\sim 5m_e$ [33]. The ICSs are delocalized and retain the orbital character of the QPSs. A distinguishable and pronounced localized in-gap state as found in highly reduced BTO (see the Supplemental Material [26]) is not observed.

Defect Dynamics.—Let us now focus on the dynamics of oxygen vacancies and their impact on the ARPES spectra. Figures 3(a) and 3(b) show low-temperature ($T \sim 100$ K) ARPES EDCs at $\overline{\Gamma}_{00}$ and $\overline{\Gamma}_{01}$ as a function of the oxygen partial pressure exposed to the sample (10^{-11} mbar $\leqslant p_{O_2} \leqslant 10^{-7}$ mbar). Whereas the intense x-ray beam used in ARPES ($\sim 10^{12}$ photons/s in the $25 \times 15\,\mu m^2$ focal spot) reduces the thin film and creates oxygen defects that populate the surface state [20,21], the O_2 gas reoxidizes the surface and continuously depletes both the QPS and the ICS. Figures 3(c) and 3(d) show low-pressure ($p \sim 10^{-11}$ mbar) ARPES EDCs, this time as a function of temperature from 80 to 380 K. Again, the spectral intensity of both QPS and ICS decreases continuously and disappears below the background level.

With no signs of surface adsorbates (see the Supplemental Material [26]), this universal response of the 2DEG to reoxidation and temperature suggests the following microscopic origin: an intricate change in the dynamic equilibrium between oxygen defects and electrons within the irradiated sample volume accompanied by a modulation of the surface band bending [34]. As localized in-gap states indicative of partially ionized defects are not observed, we assume that most oxygen vacancies are fully twofold ionized and the point defect reaction is described (in Kröger-Vink notation) by $O_O^\times \leftrightarrows V_O^{\cdot\cdot} + 2e' + \frac{1}{2}O_2$. The probability of this reaction is given by the law of mass action and is proportional to the product of the bulk concentrations of its reactants, i.e., $\propto c_{V_O^{\cdot\cdot}} n_{e'}^2 \sqrt{p_{O_2}}$. The charge neutrality condition additionally requires a net charge balance of $2n_{e'} = c_{V_O^{\cdot\cdot}}$, and the electron density $n_{e'}$ consequently scales as $p_{O_2}^{-1/6}$. Surface band bending confines the electron density $n_{e'}$ in the surface 2DEG, and the total ARPES spectral weight of QPS and ICS is thus an implicit probe of $c_{V_O^{\cdot\cdot}}$. Figure 4(a) shows ARPES intensity integrated over both spectral contributions (inset) as a function of the oxygen partial pressure. The spectral weight indeed shows the expected scaling behavior and verifies the dominant 2+ charge state of the oxygen defects in our thin films.

The temperature dependence of the integrated ARPES intensity is shown in Fig. 4(b). We observe a transition region where charge carriers are depleted exponentially with

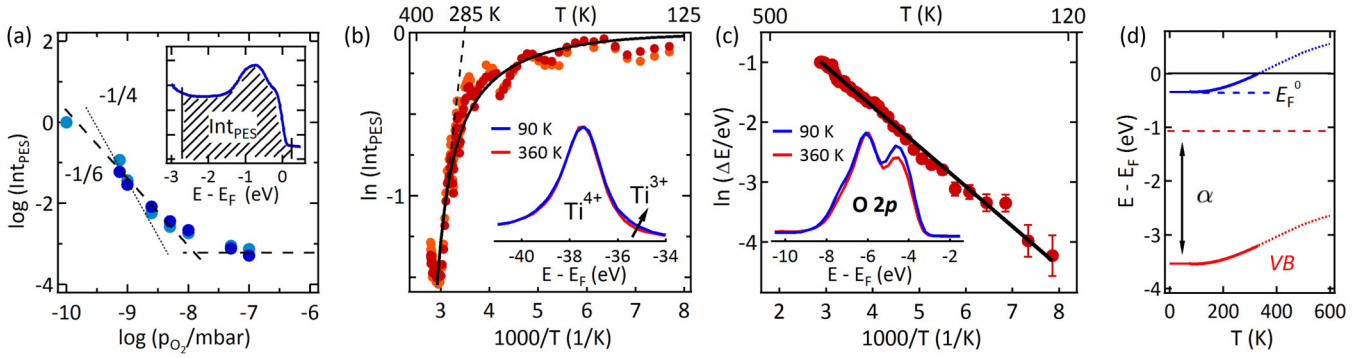

FIG. 4. (a) Integrated low-temperature ($T \sim 100$ K) ARPES intensity as a function of the oxygen partial pressure. The inset defines the integration range of $E - E_F = -2.71$ to 0.25 eV. The dashed line fits the $-1/6$ scaling behavior of +2 charged oxygen defects. The dotted line indicates the $-1/4$ scaling behavior of a +1 charge state, which is not observed in this paper. (b) Integrated low-pressure ($p \sim 10^{-11}$ mbar) ARPES intensity as a function of temperature. The black dashed line indicates the region of activated behavior. The black solid line is a fit to the carrier depletion model. The inset compares the shifted Ti $3p$ core-level line shapes at high and low temperatures. Light disks in (a) and (b) represent data from EDCs at $\overline{\Gamma}_{00}$ and dark ones from $\overline{\Gamma}_{01}$, measured with $h\nu = 135$ eV. (c) Common shift of the Ti $3s$, Ti $3p$, and O $2s$ core levels as well as the $2p$ VB states as a function of temperature. The inset compares shifted O $2p$ VB spectra at high and low temperatures. (d) Temperature-dependent rigid band bending as obtained from core-level shift (physically meaningful up to $T \sim 350$ K).

temperature. From its slope (dashed line), we determine an activation energy of $E_A \sim 0.25$ eV with an onset temperature of ~ 285 K, describing the migration barrier of electrons into the subsurface. At low temperatures, we observe a significant deviation from this scaling behavior, indicating the nonuniversality of E_A due to a temperature-dependent surface potential. This temperature-dependent band bending effect is quantified by monitoring the temperature behavior of the Ti $3s$, Ti $3p$, and O $2s$ core levels as well as the O $2p$-derived VB (see the Supplemental Material [26] for temperature-dependent core-level measurements). We find a common shift of all peaks towards higher energies, following the exponential trend $\Delta E(T) = \alpha e^{-\beta/k_B T}$ with $\alpha = 2.5$ eV and $\beta = 57$ meV depicted in Fig. 4(c).

A sketch of this shift is shown for the VB (red) in Fig. 4(d). The red dashed line marks the virtual VB pinning for $T \to \infty$, i.e., its extrapolated position for the fully oxidized surface. In a rigid band picture, the conduction band (blue) shifts by the same amount. This naturally leads to a drain of the 2DEG according to $n_e \propto k_B T \ln(1 + e^{E_F(T)/k_B T})$ (see the Supplemental Material [26] for a description of this model). The temperature-dependent position of the Fermi level with respect to the CB bottom is controlled by the band bending $E_F(T) = E_F^0 - \Delta E(T)$, where E_F^0 is the Fermi-level pinning at $T = 0$. A best fit to this model is shown as a black solid line in Fig. 4(b), appropriately describing the depletion of the 2DEG. We find a zero-temperature Fermi-level pinning of $E_F^0 \sim 0.35$ eV, consistent with the value (0.28 eV) estimated from our band-gap considerations.

Discussion.—The continuous depletion of the surface state with temperature is likely the result of a change in the dynamic equilibrium between the positively charged oxygen defects $V_O^{\cdot\cdot}$ and the negatively charged electrons e', described by (temperature-dependent) Poisson-Boltzmann theory [34]. The response to temperature is similar as the response to O_2 pressure and suggests an overall lowering of the oxygen defect concentration at the surface due to thermally and field-induced defect migration, followed by an electron redistribution. This dynamic process reduces the band bending and depletes the 2DEG until a new charge equilibrium is reached. A line-shape comparison of the Ti $3p$ core-level peak in the inset of Fig. 4(b) and of the Ti $2p$ core-level peak (see the Supplemental Material [26]) supports this scenario. A weak shoulder at low temperatures indicates Ti^{3+} oxygen defect sites, less present at high temperatures. A similar inspection of the VB region in the inset of Fig. 4(c) reveals excess spectral weight at the top and bottom of the O $2p$-derived VB at low temperatures, underlining the change in surface stoichiometry.

At first sight, this effective migration of oxygen defects into the subsurface is nonintuitive as typical activation energies are on the order of 0.6–1.2 eV [35], suggesting high diffusion onset temperatures. However, subsurface migration of oxygen defects in bulk anatase TiO_2 was indeed shown to set in at $T \sim 200$ K [36], and finite-size and interface-proximity effects can further lower the activation enthalpy in thin films [37]. We also note that the onset temperature of 285 K is remarkably close to the ferroelectric transition temperature (~280 K) between the tetragonal and the orthorhombic phases of bulk BTO [1]. But this similarity is purely coincidental in our ultrathin films as epitaxial strain pins the crystal structure over the entire temperature range and structural phase transitions are neither expected nor observed. Our results thus imply that, even below room temperature, defect migration can induce significant fluctuations of the free surface charge-carrier density in BTO. This needs to be taken into account in the fabrication of nonvolatile room-temperature applications based on BTO thin films that rely on stable (surface) conductivity. In particular, this might be important for the conception of ferroelectric devices where polarization fields can further enhance the migration of defects. In more general terms, we suggest that such defect dynamics can play a key role for the electronic response of oxide heterostructures beyond BTO and should be carefully considered.

Finally, a remarkable result of our ARPES analysis is the $p_{O_2}^{-1/6}$ scaling behavior: At low temperatures, the carrier density scaling observed in bulk crystals is typically $p_{O_2}^{-1/4}$ [dotted line in Fig. 4(a)] and attributed to accidental acceptor doping (not observed in our core-level spectra, see the Supplemental

Material [26]) or to an oxygen vacancy charge state of 1+ [38]. Localized defect states in the band gap of BTO are however clearly suppressed, and the concentration of partially ionized oxygen defects are therefore negligible. Our findings thus plausibly suggest that the 2+ charge state is the most stable and predominant ionization state in ultrathin films of BTO and provides an effective doping source up to surface carrier densities as high as 10^{14} cm^{-2} with a charge neutrality level at least 0.35 eV above the CB edge. Given the simplicity of our model, we leave the verification of these findings to further independent studies. We believe, however, that our approach paves an alternative and powerful route towards the characterization of oxygen defects by ARPES.

Acknowledgments.—We thank H. O. Jeschke for discussions and acknowledge financial support from the Deutsche Forschunsgsgemeinschaft through Project No. RE 1469/8-1 and partly from the SFB 1170 (A01). S.M. acknowledges support from the Swiss National Science Foundation under Grant No. P2ELP2-155357. Y.J.C. acknowledges support from the National Research Foundation of Korea under Grant No. NRF-2017R1C1B2004927. R.J.K. was supported by a fellowship within the Postdoc-Program of the German Academic Exchange Service (DAAD). S.U. acknowledges financial support from the Danish Council for Independent Research, Natural Sciences under the Sapere Aude Program (Grant No. DFF-4090-00125). J.S.O was supported by the Research Center Program of IBS (Institute for Basic Science) in Korea (Grant No. IBS-R009-D1) and by the ALS Doctoral Fellowships in Residence Program. This research further used resources of the Advanced Light Source, which is a DOE Office of Science User Facility under Contract No. DE-AC02-05CH11231.

[1] M. E. Lines and A. M. Glass, *Principles and Applications of Ferroelectrics and Related Materials* (Oxford University Press, Oxford, 2001), pp. 1–43.
[2] M. S. Senn, D. A. Keen, T. C. A. Lucas, J. A. Hriljac, and A. L. Goodwin, Phys. Rev. Lett. **116**, 207602 (2016).
[3] C. H. Ahn, Science **303**, 488 (2004).
[4] H. Y. Hwang, Y. Iwasa, M. Kawasaki, B. Keimer, N. Nagaosa, and Y. Tokura, Nature Mater. **11**, 103 (2012).
[5] J. Fujioka, A. Doi, D. Okuyama, D. Morikawa, T. Arima, K. N. Okada, Y. Kaneko, T. Fukuda, H. Uchiyama, D. Ishikawa, A. Q. R. Baron, K. Kato, M. Takata, and Y. Tokura, Sci. Rep. **5**, 13207 (2015).
[6] T. Sluka, A. K. Tagantsev, P. Bednyakov, and N. Setter, Nat. Commun. **4**, 1808 (2013).
[7] K. J. Choi, Science **306**, 1005 (2004).
[8] P. Ponath, K. Fredrickson, A. B. Posadas, Y. Ren, X. Wu, R. K. Vasudevan, M. Baris Okatan, S. Jesse, T. Aoki, M. R. McCartney, D. J. Smith, S. V. Kalinin, K. Lai, and A. A. Demkov, Nat. Commun. **6**, 6067 (2015).
[9] E. Y. Tsymbal, Science **313**, 181 (2006).
[10] V. Garcia, S. Fusil, K. Bouzehouane, S. Enouz-Vedrenne, N. D. Mathur, A. Barthelemy, and M. Bibes, Nature (London) **460**, 81 (2009).
[11] V. Garcia, M. Bibes, L. Bocher, S. Valencia, F. Kronast, A. Crassous, X. Moya, S. Enouz-Vedrenne, A. Gloter, D. Imhoff, C. Deranlot, N. D. Mathur, S. Fusil, K. Bouzehouane, and A. Barthelemy, Science **327**, 1106 (2010).
[12] C. Dubourdieu, J. Bruley, T. M. Arruda, A. Posadas, J. Jordan-Sweet, M. M. Frank, E. Cartier, D. J. Frank, S. V. Kalinin, A. a. Demkov, and V. Narayanan, Nat. Nanotechnol. **8**, 748 (2013).
[13] D. D. Fong, G. B. Stephenson, S. K. Streiffer, J. A. Eastman, O. Aucielo, P. H. Fuoss, and C. Thompson, Science **304**, 1650 (2004).
[14] J. Paul, T. Nishimatsu, Y. Kawazoe, and U. V. Waghmare, Phys. Rev. Lett. **99**, 077601 (2007).
[15] T. Kolodiazhnyi, M. Tachibana, H. Kawaji, J. Hwang, and E. Takayama-Muromachi, Phys. Rev. Lett. **104**, 147602 (2010).
[16] N. H. Chan, J. Electrochem. Soc. **128**, 1762 (1981).
[17] W. Meevasana, P. D. C. King, R. H. He, S.-K. Mo, M. Hashimoto, A. Tamai, P. Songsiriritthigul, F. Baumberger, and Z.-X. Shen, Nature Mater. **10**, 114 (2011).
[18] A. F. Santander-Syro, O. Copie, T. Kondo, F. Fortuna, S. Pailhès, R. Weht, X. G. Qiu, F. Bertran, A. Nicolaou, A. Taleb-Ibrahimi, P. Le Fèvre, G. Herranz, M. Bibes, N. Reyren, Y. Apertet, P. Lecoeur, A. Barthelemy, and M. J. Rozenberg, Nature (London) **469**, 189 (2011).
[19] S. M. Walker, F. Y. Bruno, Z. Wang, A. de la Torre, S. Riccó, A. Tamai, T. K. Kim, M. Hoesch, M. Shi, M. S. Bahramy, P. D. C. King, and F. Baumberger, Adv. Mater. **27**, 3894 (2015).
[20] S. Moser, L. Moreschini, J. Jaćimović, O. S. Barišić, H. Berger, A. Magrez, Y. J. Chang, K. S. Kim, A. Bostwick, E. Rotenberg, L. Forró, and M. Grioni, Phys. Rev. Lett. **110**, 196403 (2013).
[21] L. Dudy, M. Sing, P. Scheiderer, J. D. Denlinger, P. Schütz, J. Gabel, M. Buchwald, C. Schlueter, T.-L. Lee, and R. Claessen, Adv. Mater. **28**, 7443 (2016).
[22] R. Courths, Phys. Status Solidi B **100**, 135 (1980).
[23] Y. J. Chang, New Physics: Sae Mulli **64**, 15 (2014).
[24] T. C. Rödel, F. Fortuna, S. Sengupta, E. Frantzeskakis, P. L. Fèvre, F. Bertran, B. Mercey, S. Matzen, G. Agnus, T. Maroutian, P. Lecoeur, and A. F. Santander-Syro, Adv. Mater. **28**, 1976 (2016).
[25] S. Muff, N. Pilet, M. Fanciulli, A. P. Weber, C. Wessler, Z. Ristić, Z. Wang, N. C. Plumb, M. Radović, and J. H. Dil, Phys. Rev. B **98**, 045132 (2018).
[26] See Supplemental Material at http://link.aps.org/supplemental/10.1103/PhysRevMaterials.2.094411 for sample preparation, sample characterization, and details on the models.
[27] X. Chen, S. Yang, J.-H. Kim, H.-D. Kim, J.-S. Kim, G. Rojas, R. Skomski, H. Lu, A. Bhattacharya, T. Santos, N. Guisinger, M. Bode, A. Gruverman, and A. Enders, New J. Phys. **13**, 083037 (2011).
[28] S. H. Wemple, Phys. Rev. B **2**, 2679 (1970).
[29] N. C. Plumb, M. Salluzzo, E. Razzoli, M. Månsson, M. Falub, J. Krempasky, C. E. Matt, J. Chang, M. Schulte, J. Braun, H. Ebert, J. Minár, B. Delley, K.-J. Zhou, T. Schmitt, M. Shi, J. Mesot, L. Patthey, and M. Radović, Phys. Rev. Lett. **113**, 086801 (2014).
[30] Y. J. Chang, A. Bostwick, Y. S. Kim, K. Horn, and E. Rotenberg, Phys. Rev. B **81**, 235109 (2010).

[31] S. Moser, J. Electron Spectrosc. Relat. Phenom. **214**, 29 (2017).
[32] S. Moser, V. Jovic, R. Koch, L. Moreschini, J.-S. Oh, C. Jozwiak, A. Bostwick, and E. Rotenberg, J. Electron Spectrosc. Relat. Phenom. **225**, 16 (2018).
[33] W. Wunderlich, H. Ohta, and K. Koumoto, Physica B **404**, 2202 (2009).
[34] M. Kessel, R. A. De Souza, and M. Martin, Phys. Chem. Chem. Phys. **17**, 12587 (2015).
[35] W. L. Warren, K. Vanheusden, D. Dimos, G. E. Pike, and B. A. Tuttle, J. Am. Ceram. Soc. **79**, 536 (1996).
[36] P. Scheiber, M. Fidler, O. Dulub, M. Schmid, U. Diebold, W. Hou, U. Aschauer, and A. Selloni, Phys. Rev. Lett. **109**, 136103 (2012).
[37] R. A. De Souza, F. Gunkel, S. Hoffmann-Eifert, and R. Dittmann, Phys. Rev. B **89**, 241401 (2014).
[38] P. Erhart and K. Albe, J. Appl. Phys. **102**, 084111 (2007).